

Simulations of hot electron transport in radiation-ablated plasma

Bin Zhao(赵斌), Tao Tao(陶弢), Rui Yan(闫锐), and Jian Zheng(郑坚)

Citation: Chin. Phys. B, 2023, 32 (**8**): 085201. DOI: 10.1088/1674-1056/acc0f3
Journal homepage: http://cpb.iphy.ac.cn; http://iopscience.iop.org/cpb

What follows is a list of articles you may be interested in

Unstable mode of ion-acoustic waves with two temperature *q*-nonextensive distributed electrons

S Bukhari, Nadeem Hussain, and S Ali
Chin. Phys. B, 2021, 30 (**9**): 095202. DOI: 10.1088/1674-1056/abf641

Hot-electron deposition and implosion mechanisms within electron shock ignition

Wan-Li Shang(尚万里)†, Xing-Sen Che(车兴森), Ao Sun(孙奥), Hua-Bing Du(杜华冰), Guo-Hong Yang(杨国洪), Min-Xi Wei(韦敏习), Li-Fei Hou(侯立飞), Yi-Meng Yang(杨轶濛), Wen-Hai Zhang(张文海), Shao-Yong Tu(涂绍勇), Feng Wang(王峰), Hai-En He(何海恩), Jia-Min Yang(杨家敏), Shao-En Jiang(江少恩), and Bao-Han Zhang(张保汉)
Chin. Phys. B, 2020, 29 (**10**): 105201. DOI: 10.1088/1674-1056/aba9c3

Absorption of ultrashort intense lasers in laser-solid interactions

Sheng Zheng-Ming (盛政明), Weng Su-Ming (翁苏明), Yu Lu-Le (於陆勒), Wang Wei-Min (王伟民), Cui Yun-Qian (崔云千), Chen Min (陈民), Zhang Jie (张杰)
Chin. Phys. B, 2015, 24 (**1**): 015201. DOI: 10.1088/1674-1056/24/1/015201

Cylindrical and spherical Gardner solitons and double layers in a dusty electronegative nonthermal plasma with two-temperature electrons

T. Akhter, M. M. Hossain, A. A. Mamun
Chin. Phys. B, 2013, 22 (**7**): 075201. DOI: 10.1088/1674-1056/22/7/075201

Effect on Landau damping rates for non-Maxwellian distribution function consisting of two electron populations

M. N. S. Qureshi, S. Sehar, H. A. Shah, J. B. Cao
Chin. Phys. B, 2013, 22 (**3**): 035201. DOI: 10.1088/1674-1056/22/3/035201

Simulations of hot electron transport in radiation-ablated plasma

Bin Zhao(赵斌)[1,2,†], Tao Tao(陶弢)[2], Rui Yan(闫锐)[2,3], and Jian Zheng(郑坚)[2,4]

[1] *Department of Mathematics and Physics, Nanjing Institute of Technology, Nanjing* 211167, *China*
[2] *IFSA Collaborative Innovation Center, Shanghai Jiao Tong University, Shanghai* 200240, *China*
[3] *Department of Modern Mechanics, University of Science and Technology of China, Hefei* 230026, *China*
[4] *School of Nuclear Science and Technology, University of Science and Technology of China, Hefei* 230026, *China*

(Received 25 November 2022; revised manuscript received 17 February 2023; accepted manuscript online 3 March 2023)

The transport of hot electrons in inertial confinement fusion (ICF) is integrated issue due to the coupling of hydrodynamic evolution and many physical processes. A hot electron transport code is developed and coupled with the radiation hydrodynamic code MULTI1D in this study. Using the code, the slowing-down process and ablation process of the hot electron beam are simulated. The ablation pressure scaling law of hot electron beam is confirmed in our simulations. The hot electron transport is simulated in the radiation-ablated plasmas relevant to indirect-drive ICF, where the spatial profile of hot electron energy deposition is presented around the shock compressed region. It is shown that the hot electron can prominently increase the total ablation pressure in the early phase of radiation-ablated plasma. So, our study suggests that a potential-driven symmetric mechanism may occur under the irradiation of asymmetric hot electron beam. The possible degradation from the hot electron transport and preheating is also discussed.

Keywords: hot electron, ablation, indirect-drive ICF, radiation-ablated plasmas

PACS: 52.55.Pi, 52.57.–z, 52.65.–y **DOI:** 10.1088/1674-1056/acc0f3

1. Introduction

In the inertial confinement fusion (ICF) research, the generation and transport of laser produced hot electron (HE) beam are important in analyzing the physical processes of implosion, even in evaluating the success of ICF.[1] In the direct drive or indirect drive ICF scheme, a significant amount of energy can be transferred to hot electrons mainly generated by laser-plasma parametric instability (LPPI).[1,2] These hot electrons may preheat the target and reduce the compressibility due to the increase of entropy, which would degrade the target performance and the fusion ignition conditions. Therefore, the generation of hot electrons is usually undesirable and considered to be a deleterious effect on the traditional ICF, where the LPPI is expected to be kept at a lowest possible level.

Actually, hot electrons may play a beneficial role in the creation of a high ablation pressure, if hot electrons slow down on the shell's outer surface. For the earlier research on the implosion with the irradiation of CO_2 laser pulse, the transport of hot electrons is found to increase the hydrodynamic efficiency.[3] Recently, it was also shown that hot electrons play a beneficial role in creating a high ablation pressure in shock ignition conditions, where hot electrons can create several hundred Mbar (1 bar = 10^5 Pa) ablation pressure.[4] Motivated by the shock ignition research, one studied the ablation process driven by electrons theoretically and numerically, and also the processes of the shock formation with the irradiation of hot electron beam.[4–7]

As is well known, the transport of hot electrons in the ICF is an integrated problem due to the coupling of different physical processes. To simulate such processes, hot electron transport and energy deposition in the background plasma, given by hydrodynamic computation, should be investigated, then the deposited energy of hot electrons is needed to couple with the hydrodynamic evolution. In addition, the compensation return current carried by the background electrons is related to both hot electron current and hydrodynamic profile, which needs to maintain the charge and current neutrality of the plasma. The description of hot electron transport needs kinetic model, such as Vlasov–Fokker–Planck (VFP) equation, particle in cell (PIC) or Monte-Carlo method,[8–11] which usually suffer time-consuming computations or numerical complexity. A reduced kinetic model of hot electron transport has been reported in Ref. [10], which can realize rather accurate and rapid computation. In the present work, we use the reduced kinetic model to develop a hot electron transport code, which combines the radiation hydrodynamic code MULTI1D.[12] Then the slowing down process of mono-energetic electron beam is simulated to verify our code. The formation of shock wave driven by hot electrons is also simulated in the dense deuterium tritium (DT) plasma, the ablation pressure is obtained, and the corresponding scaling formula is confirmed in our simulations. Although many researches of hot electron transport for the laser-ablated plasmas have been reported, the hot electrons are rarely taken into consideration in the radiation-ablated plasmas. Here we attempt to simulate the hot electron transport in the condition of indirect drive ICF. Our simulations show that the hot electron can prominently increase the total ablation pressure for

†Corresponding author. E-mail: zhaobin@mail.ustc.edu.cn

© 2023 Chinese Physical Society and IOP Publishing Ltd

the early phase of radiation-ablated target, which may conduce to the implosion, which, however, also means that the hot electrons generated by LPPI may lead to the driven-produced asymmetry of the implosion process due to non-uniformly depositing their energy in the target capsule, such as deposition of hot electrons from laser entrance hole[13] and hohlraum wall. The possible degradation from the hot electron transport and preheating are discussed, which is helpful in analyzing the degradation of implosion performance.

2. Transport model of fast electron

The kinetic transport of hot electrons can be described by a VFP equation. In practice, the full VFP equation is very complicated to be completely solved. Based on the angular moments in the linearized VFP equation,[10] a reduced kinetic model is developed. The first two angular moments of the VFP equation are solved with a special closure relation based on the principle of the maximum angular entropy approximation from the radiative transfer theory, which can allow a rather accurate and rapid computation of the VFP distribution function with an arbitrary degree of anisotropy in momentum space. This transport model of fast electron and its numerical simulation are adopted in this work. For this reason, a brief description is given here.

The first three angular moments of hot electron distribution function f_h, are defined by $\Psi_0 = \frac{p^2}{v}\int \frac{f_\mathrm{h}\,\mathrm{d}\Omega}{v}$, $\Psi_1 = \frac{p^2}{v}\int f_\mathrm{h}\Omega\,\mathrm{d}^2\Omega$, and $\Psi_2 = \frac{p^2}{v}\int f_\mathrm{h}\Omega\otimes\Omega\,\mathrm{d}^2\Omega$, where p and $\Omega = p/p$ are the momentum of fast electron and the solid angle of propagation direction, respectively, v is the velocity of hot electron particle. Then, the VFP equation is decomposed into a set of equation of angular moments Ψ_i ($i = 0, 1, 2, \ldots$). The corresponding series of VFP expansion equation is truncated and the first two equations are given by

$$\begin{aligned}&\frac{\partial\Psi_0}{\partial t} + u\cdot\nabla\Psi_0 + \nabla\cdot(v\Psi_1)\\ =\ &\frac{\partial}{\partial\varepsilon}(v(S\Psi_0 - e\Psi_1\cdot E)),\end{aligned} \tag{1}$$

$$\begin{aligned}&\frac{\partial\Psi_1}{\partial t} + \nabla\cdot(v\Psi_2) + \frac{\partial}{\partial\varepsilon}(v(e\Psi_2\cdot E - S\Psi_1))\\ =\ &\frac{e}{p}(\Psi_0 I - \Psi_2)\cdot E - \nu_\mathrm{s}\Psi_1,\end{aligned} \tag{2}$$

where ε is the energy of hot electron particle, u is the fluid velocity, S is the electron collisional stopping power, E is the quasistatic electric field, I is the unitary tensor, and ν_s is the angular scattering coefficient from contribution of the electron–electron and electron–ion collisions. Here, the magnetic field is not considered in Eq. (2) for our one-dimensional simulation. When equations (1) and (2) are coupled and to be solved, the Ψ_2 as a function of Ψ_0 and Ψ_1 is needed for closure. The so-called M1 model is used as closure relation,

$$\Psi_2 = \frac{1}{3}\Psi_0 I + \Psi_0\mu\left(\frac{\Psi_1\otimes\Psi_1}{|\Psi_1|^2} - \frac{1}{3}I\right), \tag{3}$$

where $\mu\in[0,1]$ is as function of Ψ_0 and Ψ_1, which is obtained based on the principle of the maximum angular entropy approximation.[14]

When the distribution function (f_h) is solved, the macroscopic quantities are then obtained by integrating f_h. The integrals of two first angular moments can yield the hot electron number density $n_\mathrm{h} = \int\Psi_0\,\mathrm{d}\varepsilon$ and current density $j_\mathrm{h} = e\int v\Psi_1\,\mathrm{d}\varepsilon$. As hot electrons transport, plasma return current (j_p) will respond almost instantly to offset hot electron current, with $j_\mathrm{p} = -j_\mathrm{h}$. The generated self-consistent electric field can be determined by generalized ohmic law

$$E = -\eta j_\mathrm{h} + \frac{1}{en_\mathrm{e}}\nabla p_\mathrm{e}, \tag{4}$$

where P_e is the electron pressure of plasma, η is the plasma electrical resistivity.[9] As can be seen in Eq. (4), the self-consistent electric field is related to the hot electron kinetic transport and background plasma profile. For the hot electron transport module, equations (1) and (2) are solved by using a multigroup approach.[9,10] Actually, Ψ_0 and $v\Psi_1$ represent the number density and corresponding flux for given energy ε group, which are discretized in a staggered grid.[15] Then the advective terms in space and energy are differenced in a conservative form. In our simulation, the hot electron transport module is coupled to the Lagrangian radiation hydrodynamic code MULTI1D,[12] which has been upgraded by using the two-temperature model. The solved hydrodynamic equations in Lagrangian frame are given by

$$\frac{\mathrm{d}}{\mathrm{d}t}\rho = -\rho\nabla\cdot\boldsymbol{u}, \tag{5}$$

$$\rho\frac{\mathrm{d}}{\mathrm{d}t}\boldsymbol{u} = -\nabla(p_\mathrm{e} + p_\mathrm{i} + p_\mathrm{v}), \tag{6}$$

$$\rho C_\mathrm{vi}\frac{\mathrm{d}}{\mathrm{d}t}T_\mathrm{i} = -(p_\mathrm{i} + p_\mathrm{v})\nabla\cdot\boldsymbol{u} - \nabla\cdot\boldsymbol{Q}_\mathrm{i} + Q_\mathrm{ei}, \tag{7}$$

$$\begin{aligned}\rho\frac{\mathrm{d}}{\mathrm{d}t}E_\mathrm{e} =\ &-p_\mathrm{e}\nabla\cdot\boldsymbol{u} - \nabla\cdot\boldsymbol{Q}_\mathrm{e} - \nabla\cdot\boldsymbol{Q}_\mathrm{r}\\ &- Q_\mathrm{ei} + S_\mathrm{ext},\end{aligned} \tag{8}$$

where ρ and u are the fluid density and velocity, p_e, p_i, and p_v are the electron pressure, ion pressure, and artificial viscous pressure. Equations (7) and (8) are the conservation of ion energy and electron energy, T_i and C_vi are the ion temperature and specific heat, $\boldsymbol{Q}_\mathrm{i}$ is the classical ion heat conduction, Q_ei is the rate of energy exchange between electrons and ions, E_e and $\boldsymbol{Q}_\mathrm{e}$ are the electron specific internal energy and heat flux, respectively, and $\boldsymbol{Q}_\mathrm{r}$ is the radiation flux, which is solved with multigroup radiation diffusion. The computed energy deposition of hot electron is incorporated into the source term (S_ext)

in Eq. (8), which includes laser deposition.[12] Here, electron heat transport is modelled as flux-limited heat transport, and the flux limiter of 0.06. The real equations of state based on an input table are also included. Laser absorption is included by inverse bremsstrahlung model with the consideration of laser refraction and ray tracing. The hot electron transport of Eqs. (1) and (2) are solved in N_{sh} time substeps within one time step in hydrodynamic module, *i.e.*, a number of substeps are implemented in each hydrodynamic time step, where N_{sh} is the number of substeps for hot electron transport module. Using the time-splitting method, the total deposited energy rate of hot electrons and laser in Eq. (8) is computed after other main hydrodynamic terms have been solved. To avoid strong oscillations in the temperature in one hydrodynamic time step, the maximum relative change of T_e in all grids is controlled in the hydrodynamic module, and the time step is then adjusted. For more details about numerical implementation, readers can refer to pioneering work (Ref. [12]).

3. Numerical simulations

The slowing down of hot electron beam in a homogeneous plasma is the basic problem. We simulate it with our code as a testing case. A 1.0-MeV mono-energetic electron beam is injected into cold DT plasma with mass density 300 g/cm^3.[8] Figure 1(a) shows the hot electron distributions at times of 0 fs, 10 fs, 25 fs, 50 fs, 80 fs, and the electron average energy as a function of time is plotted in Fig. 1(b). In this case, the fast electron loses its energy by the stopping plasma and the stopping power is computed with the model of Solodov.[16] Our computed stopping time is 101.5 fs in which 90% initial energy is lost. Our computed results in Fig. 1 can be directly compared with simulations of Wu *et al.*,[17] and analytical calculations.[18]

When quite a number of fast electrons irradiate a plasma with a sufficient length in size, the deposited energy of hot electrons will ablate target and generate high pressure just like laser ablation process, which will then drive the shock wave. The ablation pressure has been calculated theoretically and simulated.[4,19,20] For instance, a fast electron beam of intensity $I = 1$ PW/cm^2 irradiates a fully ionized DT plasma with an initial uniform density of 10 g/cm^3, and an ablation pressure of about 400 Mbar is predicted by analytical formula $P_a = 175 I_{15}^{2/3} \rho_0^{1/3}$, where the intensity of I_{15} is in the unit of 10^{15} W/cm^2 and ρ_0 is the initial target density. The similar ablation processes are also investigated hereby using our present code with input hot electron intensity being $I = 1$ PW/cm^2, the initial temperature of DT plasma 1 eV, and the real equation of state based on a QEOS model[21] used. A Maxwellian energy distribution for the hot electron source is usually realistic in the LPI process of ICF. Here, the hot electron beams with Maxwellian distribution of typical temperature (T_h) are then taken as an input source from the right side.

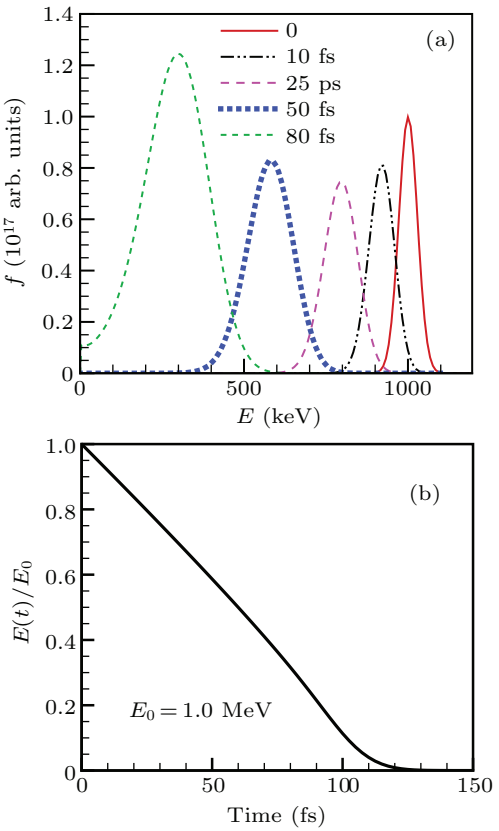


Fig. 1. (a) Curves of fast electron distribution function f (in arbitrary units) versus energy E (in unit of keV) at time $t = 0$ fs, 10 fs, 25 fs, 50 fs, 80 fs, and (b) time evolution of normalized energy.

Figures 2(a) and 2(b) give the DT target pressure and electron temperature profiles and density profiles at different time for hot electron temperature $T_h = 30$ keV, and figures 2(c) and 2(d) are for $T_h = 50$ keV. As shown in Fig. 2, the maximum ablation pressures (~ 400 Mbar) of two cases are basically the same and obviously independent of hot electron temperature. So, the computed ablation pressure are consistent with the result obtained from the scaling formula, which is then confirmed here. We also can notice that the electron beam created pressure is non-stationary. Actually, when the rarefaction wave from the right side catches up the heat front, the pressure will decrease. The time to achieve maximum pressure is called loading time t_m, which can be approximated by the time of rarefaction wave crossing through the main heated region. In the case $T_h = 30$ keV of Figs. 2(a) and 2(b), the loading time (t_m) is about $t_m \sim 100$ ps, while t_m is about ~ 250 ps for the case $T_h = 50$ keV of Figs. 2(c) and 2(d), which means that the loading time increases as the hot electron temperature T_h increases, for which the main reason is the penetration range increasing with the hot electron temperature rising. So, as indicted in Figs. 2(a) and 2(b), the temperature and pressure within the shocked range increase with time increasing for the case $t < t_m$. For the case $t > t_m$, the shock wave overtakes the heat front, and the temperature of shock front drops rapidly. Consequently, the heating of shock wave becomes apparent as indicated in Figs. 2(a) and 2(c).

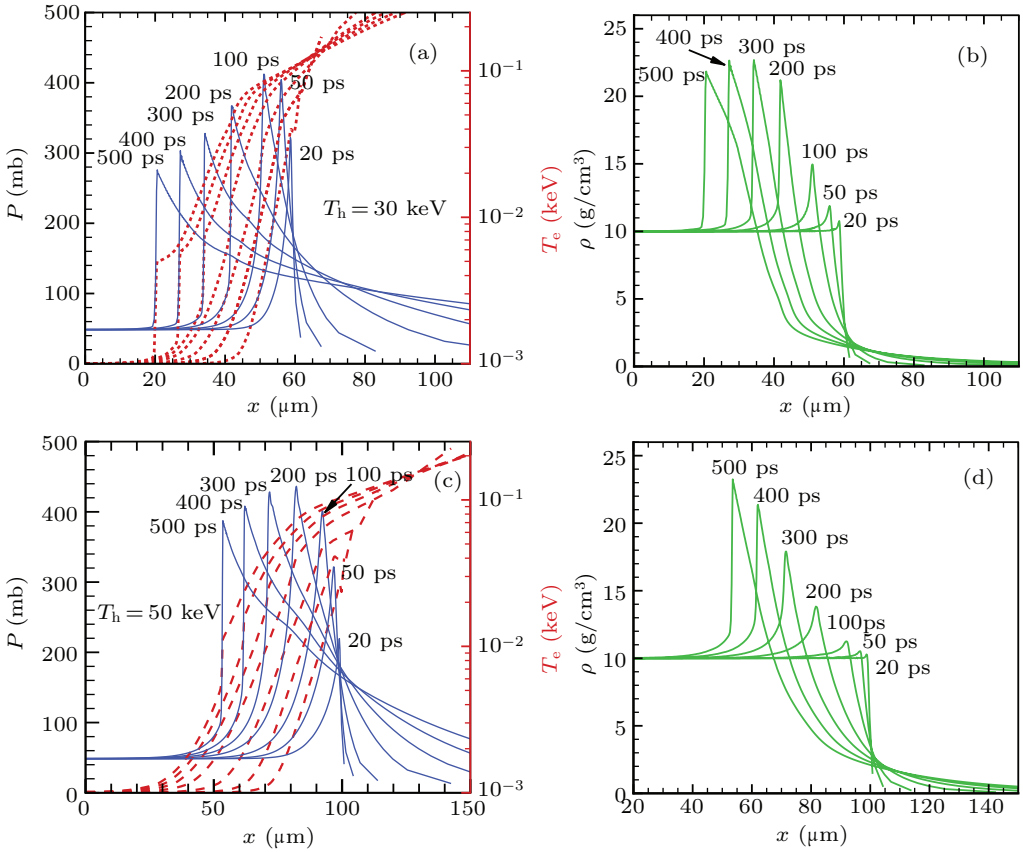


Fig. 2. (a) Pressure and DT electron temperature profiles, and (b) density profiles for DT target irradiated by a Maxwellian electron beam with temperature $T_h = 30$ keV and intensity 1 PW/cm^2. (c) Pressure and DT electron temperature profiles and (d) density profiles at temperature $T_h = 50$ keV and irradiation intensity 1 PW/cm^2.

For the evolutions of density in Figs. 2(b) and 2(d), targets are not subjected to significant compression at the beginning of the irradiation. But, the temperature gradient due to hot electron heating induces the compression motion inside the target at different velocities and boosts the shock wave growing with time. At the time of shock full formation (loading time), the maximum compression is not achieved due to high adiabat (α) of shocked region, even though the shock achieves maximum pressure. After that, the shock begins to decay slowly, while the temperature of shock front decreases rapidly since shock runs out of the hot electron deposited range. So, the maximum compression occurs later than the loading time. From the point of application of hot electron increasing ablation pressure relevant to shock ignition scheme, load time is a key parameter to choose a suitable time window for launching. The electron beam duration should not exceed several times the characteristic loading time, after which the pressure decreases.

In what follows we attempt to consider the hot electron transport in the condition of indirect drive ICF. The ablation process driven by the x-ray is computed with the consideration of the hot electron transport in the spherical configuration. Here, the hot electron beam of intensity I_e with a single-temperature Maxwellian distribution and 180° forward divergence is coupled from the outer boundary.[22] At the early stage of ablation process in the hohlraum[23] the radiation source is assumed to have a constant radiation temperature $T_r = 100$ eV for simplicity. Figure 3 shows the computed schematic target structure, x-ray radiation drive temperature (T_r), where a hot electron beam with a duration of 300 ps can be injected from the outer boundary in the simulation. Thus, the radiation ablation process with and without hot electron deposition can be compared with each other.

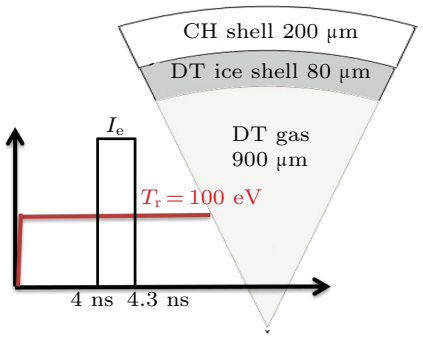


Fig. 3. Schematic target structure, x-ray radiation-drive temperature (T_r). A hot electron beam of intensity I_e can be loaded during the time between 4 ns and 4.3 ns, which is used to compare the ablation with and without hot electron deposition.

The hot electrons lose their energy during the penetration. Theoretically, the average penetration range of hot electrons with a Maxwellian distribution of temperature T_h is approximately comparable to the range of a monoenergetic beam with energy $E \simeq T_h/0.516$.[24] It can be esti-

mated that the average ranges for hot electron beams with $T_h = 30$ keV, 50 keV, 80 keV are ~ 4.7 mg/cm^2, 12.3 mg/cm^2, 29.6 mg/cm^2 in polyethylene (CH). When hot electron temperature $T_h = 30$ keV, 50 keV, 80 keV are considered in our simulations of Fig. 3, the computed hot electron deposition power and electron temperature of background plasma are compared in Fig. 4 for the input intensity $I_e = 2 \times 10^{13}$ W/cm^2 at the considered time 4.3 ns. The density profile of Fig. 4 and corresponding areal density (ρR) integrated from the origin are also presented in Fig. 5. The density profile and areal density are almost the same for different hot electron temperature because of the short irradiation time. Apparently, the areal density of CH shell exceeds 20 mg/cm^2 in Fig. 5. So, from the above analyses, the preheating in DT shell plasma and upstream CH plasmas should be negligible for the case of lower hot electron temperature, which is confirmed as shown in Fig. 4 with $T_h = 30$ keV. In one timestep of the simulation of Fig. 4, we can obtain that the ratio of energy deposited in DT shell to the total energy deposited in whole target is less than ~ 0.7 for $T_h = 50$ keV and ~ 2.2 for $T_h = 80$ keV. For this target, most of electrons deposit their energy in the CH shell, some of this energy still expends on preheating the upstream CH plasmas. At this time, the ratio of energy deposited in upstream CH plasma to the total energy deposited in whole target is obtained to be $\sim 2\%$ for $T_h = 30$ keV, 8% for $T_h = 50$ keV, and 18% for $T_h = 80$ keV. Figure 4 also illustrates the effect of preheating the upstream CH plasma located between shock front and DT–CH interface ($x = 980$ μm), in which the electron temperature of CH reaches ~ 3 eV for $T_h = 80$ keV. Of course, preheating effect in DT shell plasma and upstream CH plasma will be more prominent in the case of less areal density of CH shell. On other hand, the preheating effect decreases with shell areal density increasing in the implosion process.

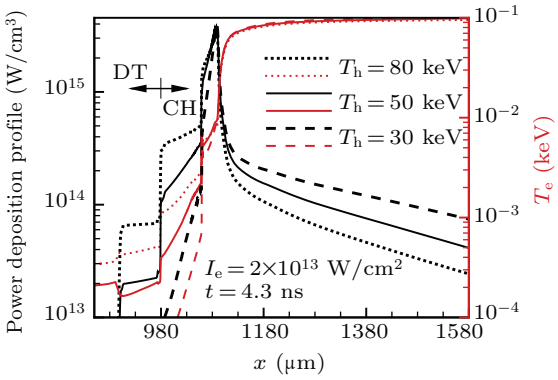


Fig. 4. Spatial profiles of hot electron deposition power and corresponding electron temperature for electron beam temperature $T_h = 30$ keV, 50 keV, and 80 keV, with input hot electron intensity $I_e = 2 \times 10^{13}$ W/cm^2 at 4.3 ns, the time which is considered in Fig. 3.

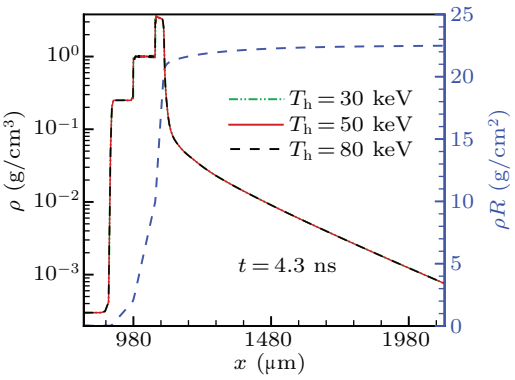


Fig. 5. Spatial density profiles of density and the corresponding areal density (ρR) integrated from the origin at 4.3 ns for Fig. 4.

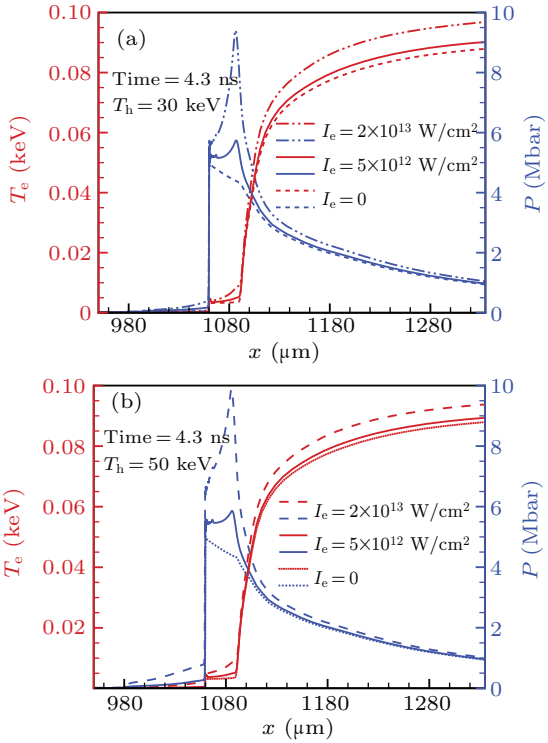


Fig. 6. The computed temperature and pressure profile at 4.3 ns with electron beams temperature (a) $T_h = 30$ keV and (b) 50 keV at different intensities $I_e = 0$, 5×10^{12}, 2×10^{13} W/cm^2.

Figure 6 shows the computed temperature profile and pressure profile near the shock at 4.3 ns with electron beam temperature $T_h = 30$ keV and 50 keV at intensity $I_e = 0$, 5×10^{12} W/cm^2 and 2×10^{13} W/cm^2. As stated above, the increase of pressure at this time can be mainly ascribed to temperature increasing due to heating by hot electron deposition. The ablation pressure without hot electron irradiation ($I_e = 0$) is about 4.9 Mbar in Fig. 6. For the different intensities of hot electron beams irradiated in combination with x-radiation source from the outer boundary, the pressure and temperature of plasma increase with the hot electron intensity within hot electron deposition range. At considered time 4.3 ns, the maximum pressure can increase to 5.7 Mbar with an intensity of $I_e = 5 \times 10^{12}$, and 9.4 Mbar with an intensity of $I_e = 2 \times 10^{13}$ W/cm^2. Those pressures are comparable to those at higher radiation temperature $T_r = 104$ eV and 120 eV according to the ablation pressure (p_a) scalling law $p_a \propto T_r^{7/2}$. Apparently, this increasing pressure is conducible to the implosion. However, the calculations also indicate that the enhancement of ablation pressure due to the asymmetrical hot

electron source might directly cause asymmetrical driving or sow the Rayleigh–Taylor (RT) seeds. These possible degradations to implosion of ICF can occur when the hot electrons are generated from laser entrance hole or hohlraum wall in the laser ablation dynamics process. A similar degradation mechanism is reported that the asymmetrical energetic ions deposited inside the capsule can result in low-mode asymmetry of implosion,[25] which are generated near the hohlraum wall/ablator interface. So, this deleterious mechanism of hot electron beams should also be taken into consideration of the integrated analysis of implosion performance.

4. Conclusions and perspectives

In summary, we use the reduced kinetic model to develop a hot electron transport code related to inertial confinement fusion, which is coupled to the radiation hydrodynamic code MULTI1D. The slowing down of hot electron beam is used to test our code. The hot electron beams ablating dense DT plasmas are simulated and analyzed, thereby confirming the scaling law of ablation pressure. It is also noticed that the maximum compression of the ablation shock occurs later than the maximum pressure when the hot electron beams with Maxwellian energy distribution are used to enhance the ablation pressure relevant to shock ignition. The ablation process driven by radiation and hot electron beam are also investigated in the typical condition of indirect drive ICF. The spatial profile of hot electron energy deposition is discussed in the considered target shell. The increase of ablation pressure are present for different input intensities (I_e) and temperature (T_h). Our studies suggest that the increasing ablation pressure due to the asymmetrical hot electron source might directly cause asymmetrical driving or generate Rayleigh–Taylor seeds, which can further degrade the implosion performance.

Acknowledgements

Project supported by the Strategic Priority Research Program of the Chinese Academy of Sciences (Grant No. XDA25050600) and the DCI joint team.

References

[1] Atzeni S and Meyer-ter-vehn J 2004 *The Physics of Inertial Fusion: Beam Plasma Interaction, Hydrodynamics, Hot Dense Matter* (Oxford: Oxford Science Pub.)
[2] Robinson A P L, Strozzi D J, Davies J R, Gremillet L, Honrubia J J, Johzaki T, Kingham R J, Sherlock M and Solodov A A 2014 *Nucl. Fusion* **54** 054003
[3] Gus'kov S Y, Zverev V V and Rozanov V B *Sov. J. Quantum Electron.* **13** 498
[4] Ribeyre X, Gus'kov S, Feugeas J L, Nicola Ph and Tikhonchuk V T 2013 *Phys. Plasmas* **20** 062705
[5] Llor Aisa E, Ribeyre X, Gus'Kov S Y and Tikhonchuk V T 2016 *Phys. Plasmas* **23** 082702
[6] Gus'kov S Y, Nicolai P, Ribeyre X and Tikhonchuk V T 2015 *JETP* **121** 529
[7] Shang W L, Che X S, Sun A, *et al.* 2020 *Chin. Phys. B* **29** 105201
[8] Wu S Z, Zhang H, Zhou C T, Wu J F, *et al.* 2015 *High Power Laser and Particle Beams* **27** 032010
[9] Chang T Q, Zhang J, Zhang J T, *et al.* 1991 *Laser plasma interaction and laser fusion* (Changsha: Hunan Scince Science and Technology Press)
[10] Touati M, Feugeas J L, Ph N, Santos J J, Gremillet L and Tikhonchuk V T 2014 *New J. Phys.* **16** 073014
[11] Delettrez J and Goldman E B 1976 *Numerical modeling of suprathermal electron transport in laser-produced plasmas*, LLE Report No. 36
[12] Zhao Y, Sheng Z, Cui Z, Ren L and Zhu J 2022 *New J. Phys.* **24** 043025
[13] Dubroca B, Feugeas J L and Frank M 2010 *Eur. Phys. J. D* **60** 301
[14] Ramis R, Schmalz R and Meyer-Ter-Vehn 1988 *J. Computer. Phys. Commun.* **49** 475
[15] Versteeg H K and Malalasekera W 2006 *An introduction to computational fluid dynamics: the finite volume method* (New York: Pearson Education)
[16] Evans R G 1983 *Laser Part. Beams* **1** 231
[17] Solodov A A and Betti R 2008 *Phys. Plasmas* **15** 042707
[18] Wu S Z, Zhang H, Zhou C T, Zhu S P and He X T 2013 *EPJ Web of Conferences* **59** 05021
[19] Robiche J and Rax J M 2004 *Phys. Rev. E* **70** 046405
[20] Llor Aisa E, Ribeyre X, Gus'kov S, Nicolaï P and Tikhonchuk V T 2015 *Phys. Plasmas* **22** 102704
[21] Nicolaï P, Feugeas J L, Touati M, Ribeyre X, Gus'kov S Y and Tikhonchuk V T 2014 *Phys. Rev. E* **89** 033107
[22] More R M, Warren K H, Young D A and Zimmerman G B 1988 *Phys. Fluids* **31** 3059
[23] Theobald W, Nora R, Seka W, Lafon M, Anderson K S, Hohenberger M, Marshall F J, Michel D T, Solodov A A, Stoeckl C, Edgell D H, Yaakobi B, Casner A, Reverdin C, Ribeyre X, Shvydky A, Vallet A, Peebles J, Beg F N, Wei M S and Betti R 2015 *Phys. Plasmas* **22** 056310
[24] Chen Y H, Li Z, Cao H, Pan K, Li S, Xie X, Deng B, Wang Q, Cao Z, Hou L, Che X, Yang P, Li Y, He X, Xu T, Liu Y, Li Y, Liu X, Zhang H, Zhang W, Jiang B, Xie J, Zhou W, Huang X, Huo W Y, Ren G, Li K, Hang X, Li S, Zhai C, Liu J, Zou S, Ding Y and Lan K 2022 *Matter Radiat. Extremes* **7** 065901
[25] Cai H B, Shan L Q, Yuan Z Q, Zhang W S, Wang W W, Tian C, Zhang F, Teng J, Yang S Q, Tang Q, Song Z F, Chen J B, Zhou W M, Gu Y Q, Zhang B H, Zhu S P and He X T 2020 *High Energy Density Phys.* **36** 100756